Cobalt–Porphyrin Catalyzed Electrochemical Reduction of Carbon Dioxide in Water. 2. Mechanism from First Principles

5 AUTHORS, INCLUDING:

Kevin Leung
Sandia National Laboratories
47 PUBLICATIONS **1,445** CITATIONS

SEE PROFILE

Na Sai
University of Texas at Austin
53 PUBLICATIONS **1,497** CITATIONS

SEE PROFILE

Craig Medforth
University of Porto
167 PUBLICATIONS **6,017** CITATIONS

SEE PROFILE

John A Shelnutt
University of Georgia
265 PUBLICATIONS **8,849** CITATIONS

SEE PROFILE

Cobalt−Porphyrin Catalyzed Electrochemical Reduction of Carbon Dioxide in Water. 2. Mechanism from First Principles

Kevin Leung,*,† Ida M. B. Nielsen,‡ Na Sai,§ Craig Medforth,‖ and John A. Shelnutt⊥

MS 1415, Sandia National Laboratories, Albuquerque, New Mexico 87185, MS 9158, Sandia National Laboratories, Livermore, California 94551, Department of Physics, University of Texas at Austin, Texas 78712, Department of Chemical and Nuclear Engineering, University of New Mexico, New Mexico 87131, and MS 1349, Sandia National Laboratories, Albuquerque, New Mexico 87185

We apply first principles computational techniques to analyze the two-electron, multistep, electrochemical reduction of CO_2 to CO in water using cobalt porphyrin as a catalyst. Density functional theory calculations with hybrid functionals and dielectric continuum solvation are used to determine the steps at which electrons are added. This information is corroborated with ab initio molecular dynamics simulations in an explicit aqueous environment which reveal the critical role of water in stabilizing a key intermediate formed by CO_2 bound to cobalt. By use of potential of mean force calculations, the intermediate is found to spontaneously accept a proton to form a carboxylate acid group at pH < 9.0, and the subsequent cleavage of a C−OH bond to form CO is exothermic and associated with a small free energy barrier. These predictions suggest that the proposed reaction mechanism is viable if electron transfer to the catalyst is sufficiently fast. The variation in cobalt ion charge and spin states during bond breaking, DFT+U treatment of cobalt 3d orbitals, and the need for computing electrochemical potentials are emphasized.

I. Introduction

CO_2 capture from flue gas and its conversion to useful products, including fuel molecules, has emerged as an important paradigm for a carbon-neutral economy.[1−4] As discussed in the preceeding paper of this series (hencefoth "paper 1"), high (∼70%) yield of carbon monoxide (CO) has been demonstrated in cobalt macrocycle-catalyzed electrochemical reduction of carbon dioxide (CO_2) in water at applied voltage of about −1.0 volt.[5−13] The relatively low electrochemical potential onset, only 0.2−0.5 V more negative than the redox potential (Φ_{redox}) of $Co^IP/Co^{II}P$ couple in water,[14] suggests that the Co^IP charge state of the catalyst is sufficient to reduce CO_2 to CO.

The mechanisms of CO_2 reduction in non-aqueous solvents, for which much more negative potentials are needed, have been examined using a variety of methods.[15−28] Co^IP-catalyzed CO_2 reduction in water and protic solvents, which requires a much less negative voltage for the onset of reaction than in organic solvent,[5−13] has received less fundamental studies. The present theoretical work focuses on the mechanism of this electrochemical reaction in aqueous media. As discussed in the preceding paper in this series (henceforth "paper 1"[29]) which examines the structures, energetics, and charge states of reaction intermediates in detail, the reaction likely takes place in the following logical sequence of steps

$$CoP + CO_2 \rightarrow CoPCO_2 \qquad (1)$$

$$CoPCO_2 + H^+ \rightarrow CoPCOOH \qquad (2)$$

$$CoPCOOH \rightarrow CoPCO + OH^- \qquad (3)$$

$$CoPCO \rightarrow CoP + CO \qquad (4)$$

"CoP" will henceforth denote cobalt porphine, the simplest porphyrin species, adopted in this work for ease of calculations.[30] Key questions to be addressed include: (1) why the reaction, which involves protonation to form carboxylate acid motifs (COOH) with pK_a typically on the order of 4.5, readily proceeds despite the fact that pH > 7 in experiments; (2) whether all steps are thermodynamically downhill; (3) whether the free energy barriers of the intermediate steps are low enough to be consistent with the observed reaction rate; and (4) at what stages the two electrons are added.

In eqs 1−4 above, we have intentionally left out the charge states of the intermediates as yet unassigned in experiments. Since the two electrons can be added at any step(s), numerous mechanisms are consistent with these equations. The sequence of electron injection is governed by the redox potentials (Φ_{redox}) of the pertinent reaction intermediates relative to the applied voltage. The half-cell potentials of various charge states of cobalt porphyrins are known,[14] but not those for the CO- and CO_2-bound complexes.

In this work, we use a combination of ab initio molecular dynamics (AIMD)[31] techniques and Density Functional Theory (DFT) calculations with various exchange-correlation functionals and the polarizable continuum model[32] (hereafter referred to as "DFT+pcm") to study eqs 1−4. These methods inform and support each other. The more economical DFT+pcm calculations approximate the aqueous environment as a dielectric continuum,[29] allowing a global overview of the entire electrochemical reaction and a survey of the numerous reaction

† MS 1415, Sandia National Laboratories, Albuquerque.
‡ MS 9158, Sandia National Laboratories, Livermore.
§ Department of Physics, University of Texas at Austin.
‖ Department of Chemical and Nuclear Engineering, University of New Mexico.
⊥ MS 1349, Sandia National Laboratories, Albuquerque.

Reduction of Carbon Dioxide in Water

J. Phys. Chem. A, Vol. 114, No. 37, 2010 **10175**

intermediates. Thus, DFT+pcm results reported in paper 1 are used to extract Φ_{redox} for all possible intermediates. Redox potentials consist of hydration free energy (ΔG_{hyd}) and ionization potential/electron affinity contributions. While Φ_{redox} and ΔG_{hyd} have also been calculated with the AIMD method and explicit treatment of the aqueous environment,[33−36] these have so far been limited to monatomic ions and molecules much smaller than porphyrins comprising a minimum of 37 atoms.[37] Our B3LYP DFT+pcm redox potentials predict that CoPCOOH⁻ is the key intermediate. To corroborate this Φ_{redox} conclusion, we also conduct more costly AIMD simulations with explicit water molecules. The hydration structures of the reaction intermediates predicted therein help explain the redox potential trends.

Next, we perform AIMD calculations on the individual reactions identified as the key steps in DFT+pcm calculations. Although it is possible that the electron addition steps of the two-electron reduction of CO_2 are rate-limiting,[12,13] modeling the electron transfer rate via Marcus theory approach[38] may not answer the most interesting scientific questions. This is because the electron injection rate almost certainly depends on engineering aspects such as the electrical contact between the gas diffusion electrode and the polymerized catalyst. Besides, it is necessary to demonstrate the viability of other steps in which electron transfer is not involved. We omit the electrode, focus on cobalt porphine molecule dispersed in water, and use AIMD to study two reactions involving [Co^{II}PCOOH]⁻: deprotonation (the reverse of eq 2) and the cleavage of the C−OH bond (eq 3). The protonation reaction proves critical to the efficient removal of one of the CO_2 oxygen atoms and reduction of the carbon atom from the +4 to the +2 formal charge state. The pK_a of [Co^{II}PCOOH]⁻ will be determined using AIMD potential of mean force (PMF) in a manner previously applied to silanol groups on silica surfaces.[39] As for the free energy change and barrier associated with the breaking of the C−OH bond (eq 3) prior to releasing CO (eq 4), there is as yet no experimental reaction rate for direct comparison. The turnover rate per catalytic active site is obscured by the undetermined proportion of active CoP molecules actually participating in the reactions. But our PMF with an approximate reaction coordinate yields a barrier which suggests that CO gas evolution should proceed readily if electron transfer from the electrode is fast. It is known experimentally that Co^{II}P binds weakly to CO;[40,41] our gas phase calculations also show that the Co^{I}P−CO complex is weakly bound. Therefore once the C−OH bond is severed to form a OH⁻, the subsequent steps (eq 4) should be exothermic, fast, and non-rate-determining, and they do not require further theoretical studies.

This work provides fundamental understanding specific to the CO_2 reduction mechanism in water using macromolecule catalysts, highlights the critical role played by the protic solvent water in lowering the voltage needed for the reaction, and may shed light on ways to further improve and modify the cobalt porphyrin catalyst. It is also of general interest to the fledgling field of computational electrochemistry. The multistep nature of the reaction emphasizes the importance of accurate calculation of redox potentials.[42−45] The protonation reaction (eq 2) is accompanied with a change in the Co ion charge state, which can be considered a form of coupled proton/electron process.[42,46] We show that this can induce hysteresis in AIMD simulations. Finally, this study in explicit water, comprising AIMD trajectories exceeding 200 ps in duration, is greatly facilitated by the use of an empirical DFT+U method[47] that can treat the localized

3d -orbitals of the Co ion accurately without resorting to more costly theoretical methods such as hybrid functionals.

This paper is organized as follows: The theoretical methods used are discussed in section II. Section III describes the redox potential predictions which determine the electron addition steps and then focuses on the deprotonation and C−O bond cleavage reactions of the key intermediate [Co^{II}PCOOH]⁻. Section IV compares the method used in the present work to our previous CO_2-related simulations;[48] it further looks to the future and briefly discusses new computational techniques that may facilitate the modeling of demanding electrochemical processes. The accuracy of electronic structure calculations which underlie our mechanistic predictions will also be addressed.[49] Section V concludes and summarizes the paper. An Appendix discusses minor hysteresis issues encountered in one part of the calculations.

II. Method

All B3LYP or PBE plus dielectric continuum calculations apply the Gaussian suite of programs version g03.[50] All DFT+U calculations use the Vienna Ab initio Simulation Package (VASP) code.[51,52] The Supporting Information document section S1 provides a brief comparison between these packages.

DFT plus dielectric continuum (DFT+pcm) calculations apply the PCM dielectric continuum model.[32] Other details are described in paper 1.[29] Zero-point energy (ZPE) contributions to eqs 2 and 3 are estimated at $T = 0$ K, also using Gaussian[50] and the 6-31+ G* basis set. The H₂O−OH⁻ complex is assumed to be the H⁺ accepting or OH⁻ containing species in ZPE calculations.

The redox potential of the A$^{(n+1)−}$/A$^{n−}$ couple is the electron affinity (EA) of A$^{n−}$ plus the difference in hydration free energies (ΔG_{hyd} difference between A$^{(n+1)−}$ and A$^{n−}$). Both EA and ΔG_{hyd} are readily obtained from DFT+pcm total free energies that include zero point energy corrections and finite temperature contributions. Where available, DFT+U Φ_{redox} is estimated by substituting ground state DFT+U energies for B3LYP ones but retaining B3LYP dielectric hydration and ZPE information. All reported Φ_{redox} are referenced to the accepted value of 4.44 V for the standard hydrogen electrode half-cell potential. The effect of the choice of DFT functionals on Φ_{redox} will be addressed in section IV.

Spin-polarized AIMD simulations apply the PBE functional, Γ-point Brillouin zone sampling, 400 eV planewave energy cutoff, deuterium masses for all protons to allow Born−Oppenheimer dynamics time steps of 0.25 fs, a $10^{−6}$ eV energy convergence criterion, and $T = 425$ K NVT conditions using a Nose thermostat. At $T = 400$ K, the PBE functional yields average pure water structure consistent with experimentally observed water $g(r)$ at $T = 300$ K.[56] Since the porphine ring exhibits significant ruffling fluctuations that explore a large configurational space, we raise the temperature by an extra 25 K to promote better sampling statistics. AIMD simulations apply 13.64 Å × 13.64 Å × 13.64 Å simulation cells which contain a CoPCOOH complex and 71 H₂O molecules.[57]

Semilocal functionals such as PBE are generally inadequate for treating first-row transition metal complexes like cobalt,[58,59] although they are more successful with transition metal dimers.[60] In general, transition metal complexes have been a challenge to DFT methods.[49] We apply the following reaction to benchmark the prediction energetics

$$[Co^{III}P]^+ + CO \rightarrow [Co^{III}P - CO]^+ \qquad (5)$$

10176 *J. Phys. Chem. A, Vol. 114, No. 37, 2010*

Leung et al.

While $Co^{II}P$ itself seems well represented by DFT functionals,[61,62] Paper 1 has shown that the widely used PBE and B3LYP functionals predict eq 5 binding energies which differ from the experimental value[41] by about 0.5 eV in opposite directions. To deal with this problem, we augment the PBE functional with DFT+U[47] applied to the partially occupied 3d orbitals of the Co ion. With a judicial choice of the U parameter, this approach has been shown to give accurate predictions for organometallic compounds, although agreement between theory and experiments has not been universal.[63-70] Using VASP PAW pseudopotentials,[52] setting $U = 2.5$ eV yields a binding energy for eq 5 that agrees with experimental data reported for the $Co^{III}TPP-CO$ complex.[29,41,71] At $T = 0$ K, these two complexes exhibit very similar VASP/PBE binding energies of 1.319 and 1.351 eV respectively; they differ by only 0.74 kcal/mol, suggesting that the experimental $Co^{III}TPP-CO$ binding free energy is a good metric for benchmarking the theoretical $Co^{III}P-CO$ predictions. As neither CO_2 nor CO strongly binds to cobalt porphyrins at most accessible Co charge states, eq 5 is the only binding constant available in the experimental literature as a benchmark. While this value of U may not be optimal for all Co charge states, referencing to eq 5 appears the most justifiable empirical route. The accuracy of AIMD simulations depends on the DFT+U method used, as will be discussed in section IV.

As reported in paper 1,[29] the optimal spin states of all gas phase B3LYP and PBE CoP complexes are low spin except $[Co^IPCOOH]^{2-}$ and the unligated $[Co^{III}P]^+$, both of which are triplets. DFT+U calculations at $T = 0$ K yield the same optimal spin states.

Equation 2 involves calculating the pK_a of $[Co^{II}PCOOH]^-$. $pK_a = -\log_{10} \exp(-\beta \Delta G^{(0)})$ has been successfully computed for molecules and surfaces in liquid water using the AIMD technique.[39,72-75] Here β is $1/k_BT$, and $\Delta G^{(0)}$ is the standard state deprotonation free energy

$$\Delta G^{(0)} = -k_B T \ln\{C_0 \int_0^{R_{cut}} dR A(R) \exp[-\beta W(R)]\}$$

(6)

C_0 denotes 1.0 M concentration, R is the reaction coordinate, $A(R)$ is a phase space factor to be discussed in section III, R_{cut} is the cutoff distance delimiting the reaction and product valleys in the free energy landscape, and $W(R)$ is the potential of mean force (PMF), referenced such that $W(R) = 0$ as $R \to \infty$. R_{cut} is taken as the onset of the plateau where $W(R) \to 0$. The umbrella sampling technique[78] and a four-atom reaction coordinate

$$R = R_1 - R_2 - R_3$$

(7)

are applied to compute $W(R)$. Here R_1 is the distance between the COOH acid proton and the oxygen atom on the designated proton-accepting H_2O, while R_2 and R_3 are the distances between this O atom and the two protons originally on the designated H_2O molecule, respectively.[39] As R_2 and R_3 are about 1.0 Å for intact O-H covalent bonds, it can be readily inferred that $R \sim -1.0$ Å is consistent with deprotonation and CO^-/H_3O^+ contact ion pair formation while $R > -0.4$ Å indicates an intact CO-H bond.[39] Designating a special H_2O molecule can be done without loss of generality because all water molecules are interchangeable and only one is at any time close enough to the acid proton to be considered a potential proton acceptor. Harmonic potentials of the form

$$U(R) = B(R - R_o)^2$$

(8)

with B values between 2 and 4 eV/Å^2 are applied to seven umbrella windows with R_o spanning the range of R to be sampled. We reference the pK_a of $[CoPCOOH]^-$ relative to the free energy of water autoionization,[73] computed using the same reaction coordinate and elevated temperature and assumed to exhibit $pK_w = 14$. As an validation test, our AIMD pK_a methodology has been applied to formic acid in water, yielding an acidity constant within a fraction of a pH unit of the experimental value (section S2 in Supporting Information).

A "reflecting boundary condition" potential $V(R_{OH})$ sets an approximate 1.2 Å distance of closest approach between water protons and the hydroxyl oxygen atom. It preserves the identity of the deprotonated -COOH (or H_2O in the case of water autoionization) by preventing proton transfer via the Grotthuss mechanism. $V(R_{OH}) = B(R_{OH} - R_1)^4$, where $B = 200$ eV/Å^4 and $R_1 = 1.3$ Å, is imposed whenever $R_{OH} < R_1$. R_{OH} is the distance between the hydroxyl (COH) oxygen and all H^+ other than the original COOH proton. Related boundary potentials have been applied to AIMD simulations of other chemical reactons.[48,76] $V(R_{OH})$ is only necessary in the deprotonation umbrella sampling window with the most negative R. As this leftmost umbrella sampling window exhibits a $W(R)$ variation of only ~ 0.6 kcal/mol (see section III), the effect of $V(R_{OH})$ should be small—much less than 0.6 kcal/mol.

For the C-OH cleavage reaction (eq 3), the reaction coordinate is taken to be R_{C-O}, the distance between the COOH carbon and the hydroxyl oxygen atom. Harmonic potentials of the form eq 8 are applied to 10 umbrella sampling windows, but with R_{C-O} replacing the four-atom coordinate R in this case. The phase space factor $A(R)$ in the free energy expression analogous to eq 6 becomes $4\pi R_{C-O}^2$.

Dealing with slow, diffusive degrees of freedom is a significant challenge in AIMD calculations of bond-breaking free energies.[48,76] During the stretching/cleavage of the C-OH bond, rotational phase factors of $k_B T \log[4\pi(R_{C-O})^2]$ should naturally emerge in well-converged evaluations of eq 3. However, rotation of the nascent product OH^- ion about the carbonyl carbon atom in water is too slow on AIMD time scales to accurately reproduce this rotational entropy. To give a better converged $W(R)$, the x and y coordinates of the carbonyl C and hydroxyl O atoms are kept identical and fixed while their z coordinates are allowed to vary. No other atom is frozen in AIMD simulations. The rotational entropy is restored by multiplying $4\pi R_{C-O}^2$ to the R_{C-O} probability distribution function at each R_{C-O}.[48,76,77] Section S3 in the Supporting Information shows that this constraint has a modest effect on the sampling of the Co-C-O angular distribution despite the bulkiness of the CoP group.

The deprotonation free energy change in eq 2 is a state function which should not depend on the reaction coordinate chosen provided that equilibrium sampling is achieved. Using the one-dimensional coordinate R, however, we observe some hysteresis due to the picosecond time scale relaxation of the charge state of the cobalt ion as the extent of deprotonation varies. For eq 3, we are interested in the free energy barrier in addition to the free energy change. Umbrella sampling yields a free energy barrier estimate which depends on and is generally underestimated by any chosen reaction coordinate because some trajectories with forward velocity can recross the "transition state" point and do not proceed to product formation.[78,79] To assess the validity of the computed barrier, we perform transmission coefficient (κ) calculations,[78,79] to be discussed in

Reduction of Carbon Dioxide in Water

J. Phys. Chem. A, Vol. 114, No. 37, 2010 **10177**

more detail below. The transition path sampling method[80] is the rigorous approach to compute free energy barriers; although more costly, it will be considered in the future. Multidimensional metadynamics,[81−83] new deprotonation coordinates,[75] the self-consistent DFT+U method,[68] and new DFT functionals[84] may also benefit future AIMD-based electrochemical calculations, and will be mentioned in section IV.

The amount of water in the simulation cell is determined using grand canonical Monte Carlo simulations at constant water chemical potential, the Towhee Monte Carlo code,[85] and the SPC/E water model.[86] The cell size is identical to that used in AIMD simulations (13.64 Å^3). The temperature is set at $T = 300$ K because the SPC/E model, unlike DFT/PBE, yields reasonable water structure at room temperature. One charge-neutral Co^{III}PCOOH is placed frozen in its DFT-optimized configuration in the simulation cell. The CoP and COOH Lennard-Jones force field parameters are approximated with those of Mn^{II}P[87] and the formate anion, respectively. The atomic partial charges are assigned using Mulliken charge analysis of a gas phase B3LYP/6-311+G(d,p) Gaussian calculation. 4×10^8 Monte Carlo moves are attempted, 30% of them being water insertion/deletions. The most probable number of water molecules in the simulation cell is determined to be 71, and this is the water content used in AIMD simulations. A net $-|e|$ charge and a neutralizing background are then imposed on the final CoPCOOH/H$_2$O configuration from the Monte Carlo run, and AIMD simulations are initiated. We choose a few sampling windows along the reaction coordinates as seed windows. With the appropriate umbrella sampling potentials of the selected windows turned on, AIMD pre-equilibration is conducted for 2 ps at $T = 500$ K. Maximally localized Wannier function analyses[88] confirm that the extra electron resides on CoPCOOH. Then the system is further equilibrated at the target temperature $T = 425$ K for another 2 ps before statistics are collected. The starting configurations for all other sampling windows are taken successively from snapshots of adjacent windows a few picoseconds into their AIMD trajectories.

The statistical uncertainty in each sampling window is estimated by splitting the trajectory into four equal parts, calculating the standard deviation for $W(R_2) - W(R_1)$, where R_1 and R_2 are the boundary values in the window, and then dividing by $4^{1/2}$ to yield an approximate error bar for the entire trajectory. The overall uncertainty convolves the standard deviations in all windows. The statistics are generated with AIMD trajectories of at least 10 ps in duration; in a few windows where the uncertainties are large, 15−20 ps AIMD runs are conducted.

The maximally localized Wannier function analysis[88] is used to determine the charge/spin state of the cobalt ion in the reactants, productions, and reaction intermediates in liquid water. As discussed in section S1 in the Supporting Information, the Mulliken charge decomposition technique, popular in the quantum chemistry community, has not been implemented in the planewave basis VASP code. Alternative charge decomposition methods such as simply integrating the charge/spin densities within some radius around the transition metal ion tend to yield ambiguous results.[89] Hence the Wannier approach appears the most useful method in our condensed phase, periodically replicated simulation cell setting.

III. Results

A. Redox Potentials, Hydration Structures, and Electronic Structures. The redox potential values are listed in Table 1. To anticipate the conclusions, we find that the predicted B3LYP

TABLE 1: Redox Potential of Various Species Using Three Functionals/Computational Methods, in Volts^a

reduced	oxidized	B3LYP	PBE	DFT+U
Co^{I}P$^-$	Co^{II}P	−1.71	−0.89	−1.46*
Co^{I}P^{2-}	Co^{I}P$^-$	−2.11	−2.31	NA
Co^{I}PCO$_2$$^{2-}$	Co^{I}PCO$_2$$^-$	−1.82	−1.78*	−1.68*
Co^{II}PCOOH$^-$	Co^{III}PCOOH	−1.17	−2.14	−1.07*
Co^{II}PCOOH^{2-}	Co^{II}PCOOH$^-$	−2.17	−2.08*	NA

^{a} ZPE values are computed using the B3LYP functional; asterisks indicate that dielectric solvation contributions also come from B3LYP. Convergence cannot be achieved when applying DFT+U to some doubly negatively charged systems in the gas phase. The electron affinities of these species are listed in section S4 of the Supporting Information. DFT+U calculations are performed using VASP; B3LYP and PBE calculations apply the Gaussian suite of codes. The Co charge state assignment in [CoPCOOH]$^-$ reflects AIMD simulations in explicit water.

DFT+pcm absolute redox potentials are not in good agreement with experimental values. However, these potentials referenced to one redox couple yield qualitative results consistent with insights gained from AIMD simulations, and they allow us to assign the charge state of the key intermediate species.

Thus, at first glance, B3LYP appears to predict a Co^{I}P/Co^{II}P redox couple value which disagrees with the average experimental value of −0.67 V (−0.5 to −0.84, depending on the porphyrin ring substituent and solvent[14]). The redox potential also strongly depends on the DFT functional used, in contrast to the findings of ref 62 for the Co^{II}P−NO/[Co^{III}P−NO]$^+$ couple. DFT+U and B3LYP redox potentials track each other while the PBE functional yields substantially different values. Systematic errors in hybrid DFT plus dielectric continuum redox potentials have been reported in the literature,[43,45] particularly those associated with the B3LYP functional.[43] While part of the discrepancy in Table 1 may be due to DFT inaccuracies, the DFT+U redox potential, fitted to eq 5, is also off by 0.8 V. Thus uncertainties arising from the use of the dielectric approximation used to calculate ΔG_{hyd} as well as the lack of ring substituents in our calculations may also be responsible. Although PBE appears to yield a Φ_{redox} for the [Co^{I}P]$^-$/Co^{II}P couple close to the experimental value, it performs worse for the benchmark reaction eq 5 than DFT+U. The result for that equation is deemed more reliable because the pertinent experiments were performed in aprotic solvents which interact weakly with the reactants.[41]

To proceed, we focus on relative B3LYP redox potential values and assume that all electrochemical measurements occur near the B3LYP [Co^{I}P]$^-$/Co^{II}P voltage. As discussed in the Introduction, this corresponds to the experimental condition where the onset of CO gas evolution is within a few tenths of a volt of the Co^{II}P reduction potential. The B3LYP redox potentials of other species relative to [Co^{I}P]$^-$/Co^{II}P (−1.71 V) then determine whether an additional electron has been incorporated at that step. A similar approach has been used in ref 43, where it has also been suggested that relative B3LYP redox potentials are much more reliable than absolute values. Thus the B3LYP functional predicts that Co^{III}PCOOH is reduced to [Co^{II}PCOOH]$^-$, while [Co^{I}P]$^-$ and [Co^{II}PCOOH]$^-$ are not reduced to [Co^{I}P]$^{2-}$ and [Co^{II}PCOOH]$^{2-}$, respectively, because their required voltages are much more negative than −1.71 V. The experimental reduction potentials for [Co^{I}P]$^-$ in aprotic solvents are indeed −0.51 to −1.2 V more negative than that for Co^{II}P.[14] However, unlike [Co^{I}P]$^-$ itself, [Co^{I}PCO$_2$]$^-$ is already reduced to [Co^{I}PCO$_2$]$^{2-}$ at the [Co^{I}P]$^-$/Co^{II}P voltage with a mere additional −0.11 V. In other words, it is much easier to add an electron to [Co^{I}PCO$_2$]$^-$ in water than [Co^{I}P]$^-$.
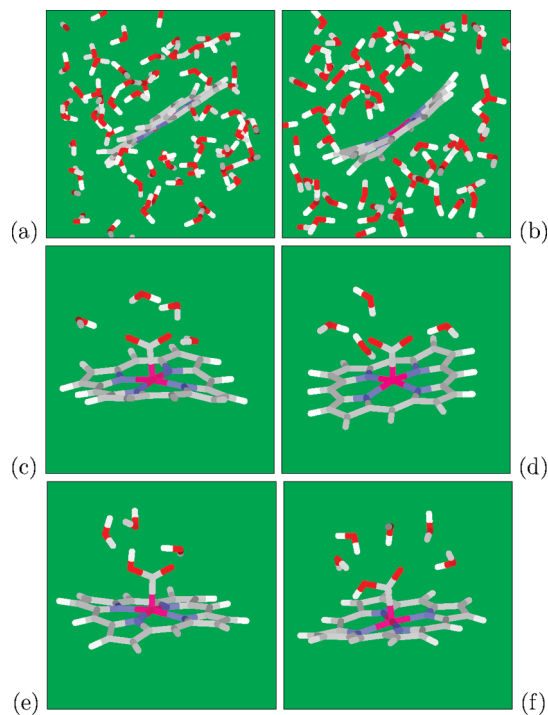
Figure 1. Snapshot of (a) $[Co^IP]^-$, (b) $[Co^IP]^{2-}$ (see footnote 91 for description of charge states), (c) $[Co^IPCO_2]^-$, (d) $[Co^IPCO_2]^{2-}$, (e) $Co^{II}PCOOH$, (f) $[Co^{II}PCOOH]^-$ in water. Panels a and b show the absence of hydrogen bonding between the negatively charged CoP and water. In panels c−f, most H_2O molecules are omitted; only those forming hydrogen bonds with the CoP structure are shown. Panels e and f depict the C−OH group in the trans (exo) and cis (endo) configuration, respectively. All snapshots are taken after 1−2 ps of short AIMD runs. Color key: pink, Co; gray, C; red, O; white, H.

Figure 2. Mechanism of CO_2 reduction with electron addition deduced from hybrid DFT plus dielectric continuum redox potential calculations. Red denotes key intermediates; green species should undergo fast reactions.

(Figure 1f). This COOH proton cannot form a hydrogen bond with other water molecules. In the gas phase, this structure is 4.93 kcal/mol more stable than the *trans* configuration where the OH points outward (Figure 1e). This feature will play a prominent role in acid−base reactions (eq 2). Intramolecular hydrogen bonds have also been suggested to facilitate CO_2 binding and chemical reduction in the literature.[2,4,24]

The calculated redox potentials (Table 1) suggest an overall mechanism shown in Figure 2. The CO_2 adsorption and the first electron insertion steps are likely simultaneous and cooperative. This is because the B3LYP functional predicts that the following equation

$$[Co^IP]^{2-} + CO_2 \rightarrow [CoP^IPCO_2]^{2-} \qquad (9)$$

exhibits a very significant free energy gain of 27 kcal/mol in water (treated as a dielectric continuum).[29] However, $[Co^IP]^-$ should not be readily reduced to $[Co^IP]^{2-}$ at or slightly below the $[Co^IP]^-$ /$Co^{II}P$ half cell voltage, and CO_2 is not strongly bound to $[Co^IP]^-$. This suggests that the CO_2 may be thought of as part of the solvent and the electron transfer to the cobalt complex as a solvent/CO_2 fluctuation-mediated process akin to the Marcus theory picture.[38] As mentioned in the Introduction, the electron transfer rate may depend on the electrical contact between the catalyst and the gas-diffusion electrode and is not the main subject of this study. The protonation and C−OH cleavage steps in Figure 2 are at the heart of the catalytic function and must be fast and spontaneous; understanding of the scientific principles involved can lead to improved catalysts and reaction conditions. In the next subsections, we consider these steps in detail using the AIMD method. $Co^{II}P$ is known to be weakly bound to CO.[40] Although experimental data are not available, B3LYP/6-31+ G* calculations indicate that the gas phase Co^IP−CO binding energy is only 1.76 kcal/mol at $T = 0$ K. Once C−OH cleavage is achieved, the rest of the reaction (eq 4) should proceed rapidly.

The Co charge and spin states predicted for B3LYP DFT+pcm optimal structures[29] and in DFT+U/AIMD aqueous phase snapshots generally agree with each other. For example, we consider an AIMD snapshot of $[Co^IPCO_2]^{2-}$:H_3O^+ contact ion pair[39] in water (Figure 3a, obtained using eq 8 with $B = 3$ eV/$Å^2$ and $R_o = -1.12$ Å).[97] A maximally localized Wannier function analysis reveals that six occupied d spin−orbitals are centered within 0.1 Å of the Co atom; another two occupied spin−orbitals are 0.86 to 0.88 Å away from the Co, and 1.04 and 1.02 Å away from the CO_2 carbon atom, respectively. (The Co−C distance is 1.90 Å in this snapshot.) This electronic configuration is consistent with a dative covalent bond donated by $[Co^IP]^{2-}$ to CO_2. The singly occupied highest occupied HOMO state is delocalized on the porphyrin ring, as has been

These trends can be explained with DFT+U/AIMD simulations in explicit water. The snapshots in Figure 1 are generated using short, 1−2 ps AIMD trajectories, which are sufficient to yield qualitative, well-equilibrated hydration structures if not highly precise average hydration numbers. Despite their net negative charges, both $[Co^IP]^-$ and $[Co^IP]^{2-}$ are effectively hydrophobic plates which do not form hydrogen bonds with water molecules;[91] no water protons are observed within 2.5 Å, a typical hydrogen bonding cutoff distance, of the porphine N and Co atoms (Figure 1a,b). This is in contrast to the charge neutral and positively charged $Mn^{II}P$ and $Mn^{III}P$, where one or two H_2O molecules strongly coordinates to the Mn site.[64] CO_2, a famously inert molecule, also fails to hydrogen bond with water.[48] However, when they combine to form $[Co^IPCO_2]^-$ and $[Co^IPCO_2]^{2-}$, the resulting complexes form four to five hydrogen bonds with water through the partially negatively charged O atoms on the CO_2, which now adopts a bent geometry like a carbonate[48,92,93] or a carboxylate anion[94,95] (Figure 1c,d). The enhanced interaction with water evidently facilitates the accommodation of an extra electron. This finding can be significant not just for electrochemical reduction of CO_2 but also for CO_2 capture in general.[96] The B3LYP DFT+pcm results reflect this CO_2^{n-} polarization information despite the fact that water is treated implicitly there.

We also consider the hydration structures of $Co^{III}PCOOH$ and $[Co^{II}PCOOH]^-$ (Figure 1e,f). The C−OH *trans* (exo) and *cis* (endo) configurations are almost isoenergetic in gas phase $Co^{III}PCOOH$, within 1.06 kcal/mol of each other. In contrast, $[CoP^{II}PCOOH]^-$ forms a strong intramolecular hydrogen bond between the COOH acid proton and one of the nitrogen atoms on the porphine ring when the proton is in the *cis* position
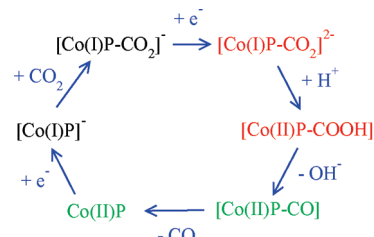
Reduction of Carbon Dioxide in Water

J. Phys. Chem. A, Vol. 114, No. 37, 2010 **10179**

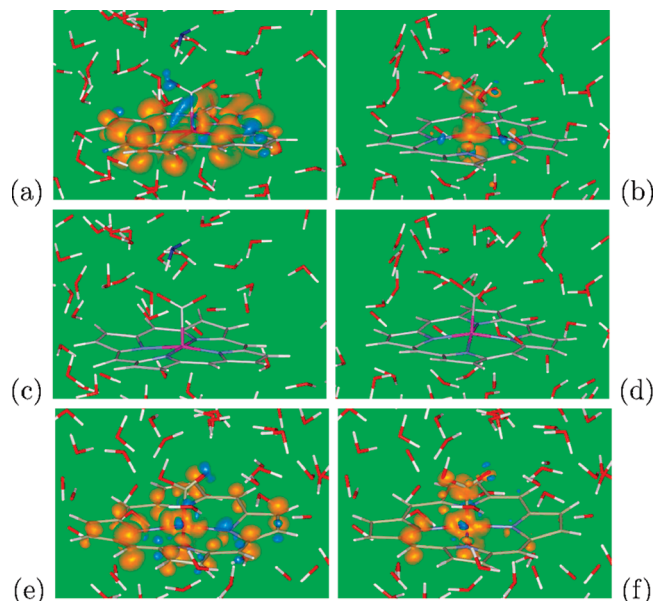**Figure 3.** Spin densities as protonation of $[Co^IPCO_2]^{2-}$ proceeds. Gold/blue: regions with net postive/negative spin densities. The isosurface spin density values are different for all panels to facilitate visualization, and are 1.32×10^{-4}, 2.88×10^{-4}, 2.32×10^{-4}, and 2.72×10^{-4} |e|/Å^3 for panels a, b, e, and f, respectively. The color scheme of the stick figures for water and CoP is as in Figure 1. (a) Well-equilibrated $[Co^IPCO_2]^{2-}$:H_3O^+ contact ion pair, obtained using a harmonic umbrella potential (eq 8) with $B = 3.0$ eV/Å, $R_o = -1.12$ Å. The singly occupied molecular orbital (HOMO) state is delocalized on the porphyrin ring. (b) $[Co^{II}PCOOH]^-$, $B = 3.0$ eV/Å, $R_o = -0.4$ Å; the harmonic potential forces a H_2O molecule to accept a hydrogen bond from the COOH proton. (c) and (d) reprise panels a and b, respectively, omitting the spin densities to reveal the atomic positions more clearly. The dark blue stick figure above CoP in panel c represents the transient H_3O^+. (e) and (f) Starting the trajectory from panel a, R_o is suddenly switched from -1.12 to -0.4 Å. The panels are taken 1.188875 and 1.189125 ps into this trajectory and bracket the transition.

discussed in paper 1 and is confirmed in the spin density plot of Figure 3a. We designate this species $[Co^IPCO_2]^{2-}$.

A key exception to the agreement between AIMD and B3LYP DFT+pcm calculations is $[Co^{II}PCOOH]^-$. Figure 3b depicts an AIMD snapshot of this species, obtained with harmonic constraint $R_o = -0.4$ Å which yields a COOH (i.e., protonated CO_2) group and also forces a H_2O molecule to accept a hydrogen bond from the COOH proton.[39] A Wannier analysis of this snapshot (Figure 3b) reveals seven occupied d spin−orbitals centered around 0.2 Å of the Co atom. Another two occupied spin−orbitals are localized along the Co−C bond, within 0.6 and 0.8 Å of the C-atom, respectively. These Wannier orbital centers are closer to C than to Co, and the electronic configuration is consistent with a $[COOH]^-$ group attached to a $[Co^{II}P]^0$. The HOMO state is a Co d orbital; the spin density of this species (Figure 3b) is far more localized than that of $[Co^IP-CO_2]^{2-}$ (Figure 3a). In contrast, B3LYP calculations with dielectric approximation for water suggest a $[Co^IP]^{2-}-COOH^+$ electronic configuration, and the HOMO is a π-orbital on the porphyrin ring there.[29] This difference most likely reflects the explicit treatment of molecular water in the DFT+U/AIMD simulation which helps to stabilize a $COOH^-$ group via hydrogen bonding. (See section S5 of the Supporting Information.) Thus inclusion of explicit water may be expected to raise the redox potential of $[CoPCOOH]^-$ and make the species even more favorable than indicated in Table 1.

The change of electronic structure coupled to protonation of $[Co^IPCO_2]^{2-}$ has consequences for AIMD simulations. Panels

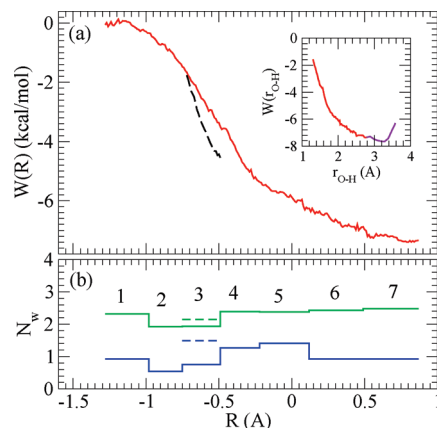**Figure 4.** (a) Red: Potential of mean force ($W(R)$) associated with $[Co^{II}PCOOH]^-$ deprotonation. The most negative values of R are associated with complete deprotonation while $R > -0.4$ Å refers to the protonated state. Inset: the violet line depicts the $\bar{W}(r_{O-H})$, computed using unbiased AIMD simulations; the red line depicts $\bar{W}(r_{O-H})$ transformed from the biased (umbrella sampling) $W(R)$ and is a cubic spline fit. (b) Hydration numbers (N_w) of the carbonyl (green) and hydroxyl (blue) oxygen atoms on the COOH group. N_w is defined as the number of water protons within 2.5 Å of these oxygen sites. Cobalt is in the Co(I) state in windows 1−3 and Co(II) in 4−7, except for the dashed curves (window 3) where Co(II) prevails. The dashed lines shows that window 3 is affected by the cobalt charge state hysteresis (see text).

e and f of Figure 3 depict the spin density transition in real time, occurring about 1.2 ps after the harmonic umbrella sampling potential (eq 8) is suddenly switched from $R_o = -1.12$ Å (consistent with that in Figure 3a) to $R_o = -0.4$ Å (Figure 3b). As alluded to above, this change in R_o leads to reprotonation of $[Co^IPCO_2]^{2-}$ from its H_3O^+ neighbor and the motion of a water molecule toward the CO_2^- group. Simultaneously, the electronic structure relaxes to $[Co^{II}PCOOH]^-$ due to the large driving force arising from the nuclear motion. However, if the driving force is not sufficient, e.g., if R_o is switched to an intermediate -0.7 Å, the system may take much longer than 1.2 ps to spontaneously sample the Co(II) charge state. As discussed below, this leads to a slight hysteresis in the umbrella sampling calculation.

B. Protonation of $[CoPCO_2]^{2-}$. Figure 4a depicts the AIMD-predicted $W(R)$ associated with the deprotonation reaction

$$[Co^IPCO_2]^{2-} + H^+ \rightarrow [Co^{II}PCOOH]^- \qquad (10)$$

Our four-atom coordinate R effectively interpolates between the large negative R deprotonated plateau region where $W(R) \rightarrow 0$, related to water-separated ion pairs,[39] and the protonated $R > -0.4$ Å region where the shallow curvature of $W(R)$ is governed by hydrogen bonding between the acid proton and a water molecule serving as a hydrogen bond acceptor. The distribution of shortest distance between a water oxygen and the COOH acid proton, obtained in an AIMD simulation of $[Co^{II}PCOOH]^-$ in water without umbrella potentials, is expressed as a free energy profile ($\bar{W}(r_{O-H})$) in the inset of Figure 4a. The optimal r_{O-H} is 3.2 Å. Recalling the definition eq 7 and the fact that R_2 and R_3 are O−H covalent bonds of lengths ~1 Å, this optimal value implies that a true minimum in $W(R)$ should not emerge until $R \sim 1.2$ Å. The optimal r_{O-H} distance is larger than the canonical hydrogen bond cutoff distance of 2.5 Å and reflects the inability of the COOH proton, engaged in a strong intramolecular hydrogen bond to one of the CoP nitrogen atoms,

to donate a hydrogen bond to water molecules (Figure 1f). Indeed, along the AIMD trajectory, there is only a 2% probability that the COOH proton and any water oxygen atoms are within 2.5 Å of each other. Fortunately, the reaction coordinate R and the umbrella constraining potentials enforce hydrogen bond donation from the acid proton to water, a prerequisite to deprotonation.

To estimate pK_a via eq 10, we find the most probable $O_{water}-H^+$ hydrogen bond distance r_{O-H} at each R, thus locally converting $W(R)$ to $\bar{W}(r_{O-H})$, and perform a spline fit to that probability distribution.[39,72] The result is matched to $\bar{W}(r_{O-H})$ in the small r_{O-H} region obtained in the aforementioned AIMD run where the umbrella potential is absent. See Figure 4a inset. Integrating over r_{O-H} with a $4\pi r_{O-H}^2$ volume element, which takes the place of the phase space factor $A(R)$ in eq 6, referencing to water autoioniziation computed at a similar elevated temperature,[39] and adding a -0.57 kcal/mol zero point energy correction estimated from gas phase B3LYP calculations, $pK_a = 9.0 \pm 0.4$ is predicted. Thus, $[Co^{II}PCOOH]^-$ does not behave like an ordinary carboxylate acid with $pK_a \sim 4.5$. The significant reduction of acidity indicates that protonation of $[Co^ICO_2]^{2-}$ is exothermic at the experimental pH >7 conditions.

In contrast, a preliminary study of the deprotonation $W(R)$ of $Co^{III}PCOOH$ reveals that $W(R)$ is almost independent of R for $R < -0.4$ Å (not shown). Our reaction coordinate has been used to calculate pK_a down to 3.8 where a finite curvature persists in $W(R)$.[39] This suggests that the pK_a of $Co^{II}PCOOH$ is less than 3.8, much lower than that of $[Co^{II}PCOOH]^-$. Thus, adding an electron to the CO_2-ligated catalyst evidently enhances its ability to hold on to excess protons.[42] While this may appear obvious in retrospect, the strong intramolecular hydrogen bonding in $[Co^{II}COOH]^-$ (Figure 1f) also likely contributes to its higher pK_a. This preliminary pK_a estimate for $Co^{III}PCOOH$ suggests that protonation of $CoPCOO^-$ cannot occur spontaneously at the experimental pH ~ 7, further confirming the B3LYP DFT+pcm Φ_{redox} prediction that $[Co^{II}PCOOH]^-$, not $[Co^{III}PCOOH]$, is the key intermediate (Figure 2).

Figure 4b shows that the hydration numbers N_w do not significantly vary with R. However, the hydration structure may determine whether hysteresis in the cobalt charge state occurs as R increases. The full curve in Figure 4 collates contributions from all windows, such that windows 1 and 3 are initiated from $[Co^IPCO_2]^{2-}$ configurations generated in a well-equilibrated window 2 trajectory, while the window 5−7 runs originate from window 4 ($[Co^{II}PCOOH]^-$). This appears to yield a smooth $W(R)$ curve. If the window 3 segment of $W(R)$ is initiated from window 4 instead, the system remains in a Co(II) state, and the dashed curve, matching poorly to the window 2, materializes. This is a classic signature of hysteresis in umbrella sampling simulations. Fortunately, only the intermediate $R_o = -0.7$ Å window 3 suffers from this problem. The maximal underestimation of $[Co^{II}PCOOH]^-$ pK_a this can introduce is the difference between the full and dashed curves in window 3, which is 0.76 kcal/mol or 0.55 pH unit. This hysteresis issue is discussed in more detail in the Appendix.

Using a purely dielectric continuum treatment of water and the B3LYP/6-31+G* method, paper 1 predicts deprotonation pK_a of 13.8 and 7.6 for $[Co^{II}PCOOH]^-$ and $Co^{III}PCOOH$, respectively. They are several pH units higher than AIMD estimates. The discrepancies are partly due to the lack of explicit water molecules in the B3LYP DFT+pcm calculations, but they also reflect the substantial (~ 5 kcal/mol) variation in deprotonation free energies when using different DFT functionals (Table 4 in paper 1).

C. C−OH Bond Cleavage Reaction. Finally, we apply umbrella sampling to study

$$[Co^{II}PCOOH]^- \rightarrow [Co^{II}PCO] + OH^- \qquad (11)$$

We use the C−O distance of the C−OH bond as the reaction coordinate. Figure 5a shows that this reaction is exothermic. Wannier analysis reveals that the system remains in the Co(II) state as R_{C-O} varies, and no hysteresis is observed. After accounting for standard state correction, the $4\pi R_{C-O}^2$ rotational contribution, a -2.5 kcal/mol ZPE correction, and integrating $\exp[-\beta W(R_{C-O})]$ in the reactant channel as in eq 6, we obtain a free energy of reaction $\Delta G^{(0)} = -8.5 \pm 1.1$ kcal/mol. The barrier height is a low $\Delta G^{(0)*} = 5.2 \pm 0.6$ kcal/mol confirms that the activation free energy is fairly low. We have not attempted to compute ZPE for $\Delta G^{(0)*}$ which requires a projecton operation that removes the reaction coordinate;[98] however, in a study of a simple C−OH bond breaking reaction,[98] ZPE has been found to be small, reducing $\Delta G^{(0)*}$ by 0.8 kcal/mol.

The predicted activation barrier may depend on the R_{CO} coordinate chosen. As in ref 48, we have computed the transmission coefficient.[78] Thus, in the umbrella sampling window containing the $W(R)$ turning point, we randomly choose 10 configurations at the top of the barrier, half with positive velocities dR_{C-O}/dt and half with negative ones, restart AIMD trajectories without umbrella sampling potentials, and determine the ratio κ that the reaction proceed without ultimate recrossing back to the reactants. $\kappa = 1$ means no recrossing and a perfectly chosen reaction coordinate. We find that $\kappa = 0.60$, indicating that R_{CO} is a reasonable coordinate and that our reported ΔG^* should be qualitatively correct. A more systematic approach is the path-sampling method,[80] which is however more computationally costly.

The C−OH cleavage activation barrier is almost a factor of 3 smaller than that previously found for the uncatalyzed $CO_3H^- \rightarrow CO_2 + OH^-$ reaction (Figure 5a inset).[48] Even though the comparison is not perfect, in that the carbon atom is not reduced to its +2 oxidation state in the previous work, the cobalt porphyrin has clearly and drastically reduced the C−OH cleavage barrier.

As the C−OH cleavage reaction proceeds, the carbonyl oxygen in the initially partially negatively charged $COOH^-$ functional group becomes part of an uncharged carbon monoxide molecule (CO) weakly bound to $Co^{II}P$, and the oxygen atom of
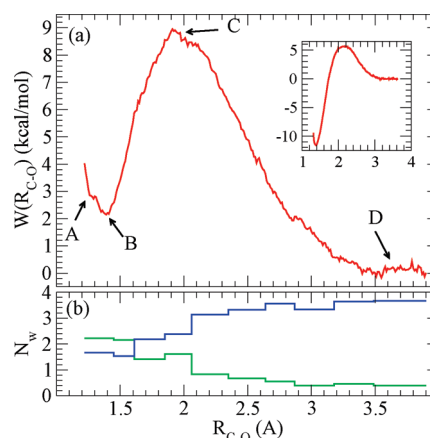

Figure 5. (a) $W(R)$ for the C−OH cleavage reaction, eq 11. Inset: $W(R)$ for $CO_3H^- \rightarrow CO_2 + OH^-$ from ref 48. Snapshots at points A−D are depicted in Figure 6. (b) Hydration numbers (N_w) for the carbonyl (green) and hydroxyl (blue) oxygen atoms as R_{C-O} varies.

Reduction of Carbon Dioxide in Water

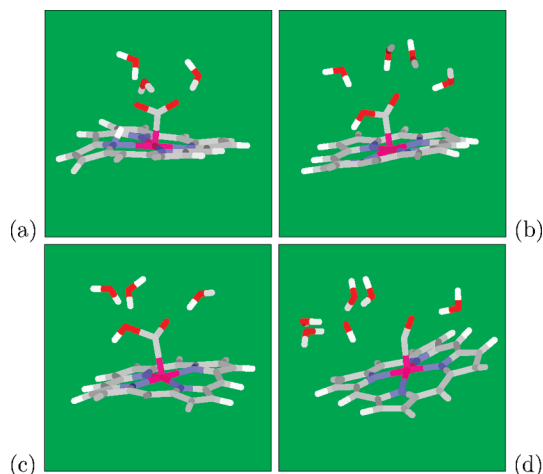*J. Phys. Chem. A, Vol. 114, No. 37, 2010* **10181**

Figure 6. (a−d) Snapshots in the four umbrella sampling windows indicated in Figure 5. AIMD simulations are conducted in an explicit liquid water environment; only a few water molecules are shown in these snapshots. In panel a, the proton on the COOH group has migrated to one of the nitrogen atoms on the porphyrin ring. The color scheme is as in Figure 1.

the nascent CO exhibits a hydration number N_w which steadily decreases (Figure 5b). In contrast, the hydroxyl oxygen transitions toward a hydroxide anion (OH^-), and its N_w increases to about 3.5. The N_w value for the emerging OH^- oxygen in the present heterogeneous environment is therefore similar to that predicted in bulk liquid water using the PBE functional.[99] Figure 6 further depicts snapshots of the instantaneous hydration structure of the COOH group at different values of the reaction coordinate. Panel b represents a configuration where the COOH proton is intramolecularly hydrogen bonded to a porphine ring N atom (Figure 1f). In panel a, which corresponds to a kink in Figure 5a, the COOH proton has instantaneously been donated to a N atom, forming a covalent bond with it. In the gas phase, this N−H bonded structure is 6.68 kcal/mol higher in energy than that of Figure 6b. Nevertheless, in the aqueous phase, this configuration is occasionally observed.

IV. Discussion

A. Comparison with Previous CO₂ Theoretical Work. In this subsection, we make comparisons with some computational aspects of ref 48 and with paper 1.[29]

Unlike ref 48, we have not constrained the OH bond rotation around the C−O axis in the cleaved COOH group and then corrected for the entropic contributions there. This is because the PBE functional we use is consistent with much faster OH^- dynamics in water than the RPBE functional previously applied,[48,99,100] and it is reasonable to assume that the OH rotation around the C−O axis is better-sampled than in RPBE simulations within 10 ps AIMD trajectories. This should only affect $\Delta G^{(0)}$, not $\Delta G^{(0)*}$, because the C−OH bond is not completely broken at the transition state at $R_{C-O} = 1.9$ Å and free OH rotation around the C−O axis does not occur there. The important qualitative conclusion of this work is that $\Delta G^{(0)}$ is exothermic and that C−OH bond breaking is thermodynamically downhill; the precise free energy change associated with eq 11 is less important.

We have not attempted to correct the AIMD/DFT+U $W(R)$ with single point MP2 calculations as was done in ref 48. The CoP systems examined in this work are too large for large-basis MP2. Furthermore, in ref 48 the DFT functional used was RPBE,[100] which is arguably less accurate for heterogeneous C−O bond breaking than the PBE functional used herein.

Unlike paper 1, we have focused on eq 3 and not the proton-assisted variation

$$[Co^{II}PCOOH]^- + H^+ \rightarrow Co^{II}PCO(OH_2)$$

$$Co^{II}PCO(OH_2) \rightarrow [Co^{II}PCO] + H_2O \qquad (12)$$

Thermodynamically the two are equivalent.[30] In terms of kinetics, which paper 1 does not deal with, they will have different activation barriers. To estimate $\Delta G^{(0)*}$ for eq 12, we note that all AIMD $W(R)$ reported for protonation/deprotonation reactions in the literature have been monotonic; i.e., the free energy changes and activation barriers are the same. Assuming the second half of eq 12 is also fast to the point of being barrierless, which gives a lower limit on the overall eq 12 barrier, $\Delta G^{(0)*}$ for eq 4 would be entirely due to the $\Delta G^{(0)}$ of the first half of this equation and related to the pK_a of $Co^{II}PCO(OH_2)$. At the pH = 7 experimental conditions, the pK_a of the C−OH_2 group in $Co^{II}PCO-OH_2$ will have to be above 3.2 in order to have a lower barrier than the $\Delta G^* = 5.2$ kcal/mol we find for eq 3. This appears unlikely; C−OH_2 groups tend to be very acidic and lose protons readily. In any case, if this alternate, proton-assisted route of C−O cleavage were faster, the barrier estimated in our PMF calculation (Figure 5) would be an upper bound to the reaction activation free energy; the C−O bond breaking step would still exhibit fast dynamics, and the qualitative conclusion of this paper would be unchanged. We plan to revisit eq 12 in the future.

B. Alternative Computational Methods. A two-dimensional PMF calculation should remove the hysteresis behavior in the protonation reaction (eq 11, Figure 4). A convenient second variable may be the hydration number of the O atom in the OH group. This is because the black dashed curve in Figure 4a exhibits $N_w = 1.49$ for that oxygen, considerably higher than the $N_w = 0.75$ for the red, well-behaved $W(R)$ segment, suggesting that the electronic structure is correlated with the average hydration number. 2-D PMF simulations would be substantially accelerated using the metadynamics method[81−83] over traditional umbrella sampling.

Our pK_a calculations suggest that deprotonation of weak acid groups which exhibit intramolecular hydrogen bonding and do not donate hydrogen bond to water may require the use of a large number of sampling windows. This difficulty may be circumvented by reversibly annihilating the proton using an artificial reaction pathway[75] in a what might be called a "molecular grand canonical Monte Carlo" approach.[101] This method does introduce the disadvantage of changing the net charge in the finite-sized simulation cell and may require a number of new conformational constraints.

Finally, the self-consistent DFT+U approach[68] has been tested for eq 5. This method has the potential to establish a U value without resorting to parametrization with experimental results. Our preliminary studies suggest that this approach yields a $Co^{III}P-CO$ binding energy that may be somewhat too small, but further development of this promising approach is under way.[102]

The above theoretical considerations, touching on many newly developed techniques, emphasize the complexity and challenges associated with modeling electrochemical reactions in aqueous phase, explicit water simulations.

C. Accuracy of DFT Functionals and Redox Potentials. Accurate DFT functionals and dielectric continuum approximation of the aqueous solvent are critical for DFT+pcm determi-

nation of redox potentials,[43−45,90] which in turn govern the viable reaction intermediates and the overall reaction mechanism. We have so far considered PBE, B3LYP, and DFT+U electronic structure methods with the U parameter in DFT+U fitted to an experimental binding constant (Table 1). B3LYP and DFT+U redox potentials track each other and should predict the same reaction mechanism at voltages slightly more negative than the Co[I]P/Co[II]P couple. In contrast, the PBE functional predicts that [Co[II]COOH]$^-$ is extremely unstable with respect to the far more acidic [Co[III]COOH] complex near the PBE Co[I]P/Co[II]P redox potential. The B3LYP Φ_{redox} predictions are more consistent with AIMD hydration structure considerations and the fact that the CO_2 reduction reaction readily occurs near neutral pH in a carbonate buffer (section III).

More accurate DFT functionals may be used in the future to further examine the mechanism proposed herein. Candidates include the M06 class of functionals designed to yield better thermochemistry accuracy for transition metal complexes,[84] the B4(XQ3)LYP functional which has been found to yield improved redox potentials for a suite of test cases,[45] and Gutzwiller wave function based methods.[103] The quality of the PCM dielectric continuum model[32] should also be further examined.[43]

V. Conclusions

In this work, we have applied first principles calculations to examine the mechanism of the multistep, two-electron electrochemical reduction of CO_2 to CO in water using cobalt porphyrin (CoP) as catalyst. First we have extracted redox potentials using the B3LYP functional and a dielectric continuum treatment of water.[29] Even though the absolute value for the [Co[I]P]$^-$/Co[II]P couple is not in good agreement with experiments, the relative values of various redox potentials allow us to determine where the electron transfers occur among the four intermediate steps. Due to the enhanced interaction of CO_2 with water when bound to cobalt porphine, [Co[I]PCO$_2$]$^{2-}$ and [Co[II]PCOOH]$^-$ are the key intermediates. This finding may be useful not just for electrochemical reduction of CO_2 but for CO_2 capture from flue gas as well.

AIMD umbrella sampling calculations show that the pK_a associated with [Co[II]PCOOH]$^-$ deprotonation is about 9.0. This indicates that the protonation of [Co[I]PCO$_2$]$^{2-}$ is downhill at the bicarbonate buffer experimental conditions (pH $\sim$ 7). The subsequent cleavage of the C−OH bond is also exothermic, and the activation free energy involved is estimated to be only 5.2 kcal/mol. If we assume a vibrational prefactor of $k = 0.1$ ps^{-1}, C−OH cleavage should occur in nanosecond time scale at $T = 300$ K. Hence two key steps in the multistep reaction should proceed readily, and it is likely that the electron transfer between the gas diffusion electrode and the polymerized porphyrin catalyst is the rate-limiting step of the CO_2 to CO reduction reaction in water.[5−13]

Hysteresis in the Deprotonation AIMD Simulation. This Appendix discusses in more detail the hysteresis behavior during pK_a PMF calculations (window 3 in Figure 4).

As mentioned in section II, all AIMD trajectories ultimately originate from a Monte Carlo simulation-equilibrated classical force field configuration where a CoPCOOH is fixed in a gas phase optimized, intramolecularly hydrogen-bonded geometry (Figure 1f). The [Co[II]PCOOH]$^-$ is immersed in water and equilibrated using AIMD at several stretched values of the reaction coordinates associated with eq 10 and eq 11 using harmonic potentials $U(R)$ (eq 8).

During the equilibration run for the deprotonated window 2 of Figure 4, we impose $R_o = -1.12$ Å on the initial [Co[II]PCOOH]$^-$ system, which turns into a [Co[I]PCO$_2$]$^{2-}$:H$_3$O$^+$ contact ion pair within 1 ps. A maximally localized Wannier function analysis of an AIMD snapshot confirms that, in this ion pair, Co has spontaneously switched to the +I charge state which should be favored for large negative R. Therefore the AIMD trajectory in window 2 (and that in window 1, spawned from window 2) yields an unambiguous Co(I) charge state. Likewise, windows 4−7 are spawned successively from a window 4 trajectory equilibrated using $R_o = -0.4$ Å, and they reflect a Co(II) charge state which is favorable in this R range. An additional test further confirms that the Co(II) charge state spontaneously occurs at less negative R. We start with a [Co[I]CO$_2$]$^{2-}$, $R_o = -1.12$ Å configuration in a equilibrated window 2 trajectory and abruptly switch to $R_o = -0.4$ Å (i.e., effectively jumping from window 2 to window 4 in Figure 4). [Co[II]PCOOH]$^-$ is recovered within 1.2 ps, consistent with the Co(II) charge state observed in the window 4 trajectory which originally started out as [Co[II]PCOOH]$^-$. The change in electronic structure in real time, represented by the changes in the spatial distribution of the spin density, is depicted in Figure 3. Thus, after an approximately 1 ps equilibration run, the final Co charge state becomes independent of initial conditions.

Only window 3, located in the Co(I)/Co(II) transition region, exhibits a strong dependence on initial conditions. We have initially started from a snapshot in window 4 and then switched $R_o = -0.4$ Å to $R_o = -0.7$ Å. The latter value of R_o does not apparently contain sufficient driving force to rapidly alter the Co charge state, and the system remains [Co[II]PCOOH]$^-$ throughout the 10 ps sampling trajectory. This yields the dashed $W(R)$ segment in Figure 4a which exhibits a slope at the window edge that matches poorly to the window 2, [Co[I]PCO$_2$]$^{2-}$:H$_3$O$^+$ contribution. To make progress, we restart the window 3 simulation from a snapshot of window 2, abruptly switch the umbrella potential from $R_o = -1.12$ Å there to $R_o = -0.7$ Å, equilibrate for 1 ps, and collect statistics for 10 ps. The system remains in the Co(I) charge state throughout the trajectory. The corresponding $W(R)$ segment in window 3 (full curve in Figure 4a) matches reasonably well with those in windows 2 and 4 and is taken to be the final result.

An ergodic AIMD simulation should in principle spontaneously sample both Co(I) and Co(II) charge states. Thus, the correct $W(R)$ in this intermediate R region should be a weighted average of the full and dashed curves. Apparently the statistical weight for Co(I) is much larger, so that only including Co(I) $W(R)$ information already yields a smooth $W(R)$ curve in Figure 4.

A secondary, less signficant type of hysteresis associated the position of the COOH proton also becomes apparent in Figure 7. When the COOH group is intact, and no H$_2$O accepts a hydrogen bond from the COOH proton, the hydroxyl group intramolecularly hydrogen bonds to a N atom on the porphine

Reduction of Carbon Dioxide in Water

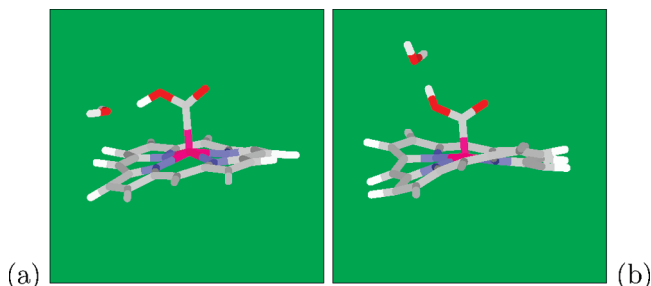*J. Phys. Chem. A, Vol. 114, No. 37, 2010* **10183**

Figure 7. Panels a and b correspond to the solid and dashed line in window 3, respectively. The color scheme is as in Figure 1.

ring in a *cis* configuration (Figure 1f). Enforcing $U(R)$ with $R < 0.5$ Å imposes COOH–H_2O hydrogen bonding that breaks this intramolecular coupling (Figure 7a). When R is further reduced to $R \sim -1$ Å, the [COOH]$^-$ proton is detached from the hydroxyl oxygen, landing on the hydrogen-bonding-accepting H_2O molecule. This newly formed H_3O^+ spontaneously migrates away from the hydrophobic porphine ring and coordinates to what is now a $CO_2^{\delta-}$ group in the axial (*trans*) position. Now the excess proton sticks out of the porphine plane. When we increase R_o to reprotonate the COOH group, the system remains in this isomeric form (Figure 7b). Isomerization between the two may entail a free energy barrier of several kcal/mol even for a stretched O–H, and does not occur on AIMD time scales in window 3. The lack of isomerization should have no significant effect on the $W(R)$ of window 3; while the gas phase Figure 1f [Co^{II}PCOOH]$^-$ intramolecular hydrogen bonded configuration is stabilized over the Figure 1e isomer by about 4.93 kcal/mol, that hydrogen bond is already broken when the carboxylate proton donates a hydrogen bond to a water molecular (Figure 7a). This secondary hysteresis may be avoided altogether using an artificial deprotonation coordinate,[75] although it is not obvious the electronic hysteresis will be avoided as well.

Supporting Information Available: Further information regarding differences between the VASP and Gaussian packages, formic acid pK_a calculation as a benchmark of the reaction coordinate used in this paper, the distribution Co–C–H angles in AIMD simulations, gas phase electron affinities of reaction intermediates, and cobalt charge state in CoPCOOH$^-$ in implicit versus explicit solvent environment. This information is available free of charge via the Internet at http://pubs.acs.org/.

References and Notes

(1) Arakawa, H.; Aresta, M.; Armor, J. N.; Barteau, M. A.; Beckman, E. J.; Bell, A. T.; Bercaw, J. E.; Creutz, C.; Dinjus, E.; Dixon, D. A.; Domen, K.; DuBois, D. L.; Eckert, J.; Fujita, E.; Gibson, D. H.; Goddard, W. A.; Goodman, D. W.; Keller, J.; Kubas, G. J.; Kung, H. H.; Lyons, J. E.; Manzer, L. E.; Marks, T. J.; Morokuma, K.; Nicolas, K. M.; Periana, R.; Que, L.; Rostrup-Nielson, J.; Sachtler, W. M. H.; Schmidt, L. D.; Sen, A.; Somorjai, G. A.; Stair, P. C.; Stults, B. R.; Tumas, W. *Chem. Rev.* **2001**, *101*, 953.
(2) Benson, E. E.; Kubiak, C. P.; Sathrum, A. J.; Smieja, J. M. *Chem. Soc. Rev.* **2009**, *38*, 89.
(3) Chaplin, R. P. S.; Wragg, A. A. *J. Appl. Electrochem.* **2003**, *33*, 1107.
(4) Fujita, E. *Coord. Chem. Rev.* **1999**, *185*, 373.
(5) Furuya, N.; Matsui, K. *J. Electroanal. Chem.* **1989**, *271*, 181.
(6) Ryba, G.; Shelnutt, J.; Prarie, M. R.; Assink, R. A. *Sandia Natl. Lab. [Tech. Rep.] SAND* **1997**, SAND-97-0414.
(7) Sonoyama, N.; Kirii, M.; Sakata, T. *Electrochem. Commun.* **1999**, *1*, 213.
(8) Magdesieva, T. V.; Yamamoto, T.; Tryk, D. A.; Fujishima, A. *J. Electrochem. Soc.* **2002**, *149*, D89.
(9) Magdesieva, T. V.; Butin, K. P.; Yamamoto, T.; Tryk, D. A.; Fujishima, A. *J. Electrochem. Soc.* **2003**, *150*, E608.
(10) Ramirez, G.; Ferraudi, G.; Chen, Y.-Y.; Trollund, E.; Villagra, D. *Inorg. Chim. Acta* **2009**, *362*, 5.
(11) Ramirez, G.; Lucero, M.; Riquelme, A.; Villagran, M.; Costamagna, J.; Trollund, E.; Aguirre, M. J. *J. Coord. Chem.* **2004**, *57*, 249.
(12) Dreyse, P.; Ramirez, G.; Riquelme, A.; Isaacs, M. *J. Chil. Chem. Soc.* **2006**, *51*, 923.
(13) Riquelme, M. A.; Isaacs, M.; Lucero, M.; Trollund, E.; Aguirre, M. J. *J. Chil. Chem. Soc.* **2003**, *48*, 89.
(14) The Co^{II}P reduction potential varies from−0.50 to−0.84 V as the solvent and ring substituents are altered. See: Kadish, K. M.; Royal, G.; Van Caemelbecke, E.; Gueletti, L. In *The Porphyrin Handbook*; Kadish, K. M., Smith, K. M., Guilard, R., Eds.; Academic Press: Boston, 2000; Vol. 9, pp 1−219.
(15) Grodkowski, J.; Neta, P.; Fujita, E.; Mahammed, A.; Simkhovich, L.; Gross, Z. *J. Phys. Chem. A* **2002**, *106*, 4772.
(16) Grodkowski, J.; Neta, P. *J. Phys. Chem. A* **2000**, *104*, 4475.
(17) Grodkowski, J.; Neta, P. *J. Phys. Chem. A* **2000**, *104*, 1848.
(18) Grodkowski, J.; Dhanasekaran, T.; Neta, P.; Hambright, P.; Brunschwig, B. S.; Shinozaki, K.; Fujita, E. *J. Phys. Chem. A* **2000**, *104*, 11332.
(19) Dhanasekaran, T.; Grodkowski, J.; Neta, P.; Hambright, P.; Fujita, E. *J. Phys. Chem. A* **1999**, *103*, 7742.
(20) Behar, E.; Dhanasekaran, T.; Neta, P.; Hosten, C. M.; Ejeh, D.; Hambright, P.; Fujita, E. *J. Phys. Chem. A* **1998**, *102*, 2870.
(21) Fujita, E.; Furenlid, L. R.; Renner, M. W. *J. Am. Chem. Soc.* **1997**, *119*, 4549.
(22) Ogata, T.; Yanagida, S.; Brunschwig, B. S.; Fujita, E. *J. Am. Chem. Soc.* **1995**, *117*, 6708.
(23) Matsuoka, S.; Yamamoto, K.; Ogata, T.; Mitsuhiro, K.; Nakashima, M.; Fujita, E.; Yanagida, S. *J. Am. Chem. Soc.* **1993**, *115*, 601.
(24) Fujita, E.; Creutz, C.; Sutin, N.; Brunschwig, B. S. *Inorg. Chem.* **1993**, *32*, 2657.
(25) Creutz, C.; Schwarz, H. A.; Wishart, J. F.; Fujita, E.; Sutin, N. *J. Am. Chem. Soc.* **1991**, *113*, 3361.
(26) Fujita, E.; Creutz, C.; Sutin, N.; Szalda, D. J. *J. Am. Chem. Soc.* **1991**, *113*, 343.
(27) Creutz, C.; Schwarz, H. A.; Wishart, J. F.; Fujita, E.; Sutin, N. *J. Am. Chem. Soc.* **1989**, *111*, 1153.
(28) Morris, A. J.; Meyer, G. J.; Fujita, E. *Acc. Chem. Res.* **2009**, *42*, 1983.
(29) Nielsen, I. M. B.; Leung, K. *J. Phys. Chem. A* DOI: 10.1021/jp101180m.
(30) Unlike Paper 1,[29] eq 3 is written without a second proton; it is trivially related to the CoPCOOH + H$^+$ → CoPCO + H$_2$O reaction studied in paper 1 via the pK_w of water.
(31) Car, R.; Parrinello, M. *Phys. Rev. Lett.* **1985**, *55*, 2471.
(32) Barone, V.; Cossi, M.; Tomasi, J. *J. Chem. Phys.* **1997**, *107*, 3210.
(33) Leung, K.; Rempe, S. B.; von Lilienfeld, O. A. *J. Chem. Phys.* **2009**, *130*, 204507.
(34) Seidel, R.; Faubel, M.; Winter, B.; Blumberger, J. *J. Am. Chem. Soc.* **2009**, *131*, 16127.
(35) Costanzo, F.; Sulpizi, M.; Della Valle, R. G.; Sprik, M. *J. Chem. Theory Comput.* **2008**, *4*, 1049.
(36) Migliore, A.; Sit, P.H.-L.; Klein, M. L. *J. Chem. Theory Comput.* **2009**, *5*, 307.
(37) At these system sizes, even application of the quasi-chemical theory, which treats part of the solvent shell explicitly, may become costly. See, e.g.: Asthagiri, D.; Pratt, L. R.; Paulaitis, M. E.; Rempe, S. B. *J. Am. Chem. Soc.* **2004**, *126*, 1285. Rogers, D. M.; Beck, T. L. *J. Chem. Phys.* **2008**, *129*, 4505.
(38) Marcus, R. A. Sutin, N. *Biochim. Biophys. Acta* **1984**, *81*, 511.
(39) Leung, K.; Nielsen, I. M. B.; Criscenti, L. J. *J. Am. Chem. Soc.* **2009**, *131*, 18358.
(40) Hu, Y.; Han, B. C.; Bao, L. Y.; Mu, X. H.; Kadish, K. M. *Inorg. Chem.* **1991**, *30*, 2446.
(41) Mu, X. H.; Kadish, K. M. *Inorg. Chem.* **1989**, *28*, 3743.
(42) See, e.g., the theoretical Pourbaix diagram correlating pH with redox potentials in: Muckerman, J. T.; Polyansky, D. E.; Wada, T.; Tanaka, K.; and Fujita, E. *Inorg. Chem.* **2008**, *47*, 1787.
(43) Roy, L. E.; Jakubikova, E.; Guthrie, M. G.; Batista, E. R. *J. Phys. Chem. A* **2009**, *113*, 6745.
(44) Winget, P.; Cramer, C. J.; Truhlar, D. G. *Theor. Chem. Acc.* **2004**, *112*, 217.
(45) Galstyan, A.; Knapp, E. W. *J. Comput. Chem.* **2009**, *30*, 203.
(46) Edwards, S. J.; Soudackov, A. V.; Hammes-Schiffer, S. *J. Phys. Chem. B* **2009**, *113*, 14545, and references therein.
(47) Anisimov, V. I.; Zaanen, J.; Andersen, O. K. *Phys. Rev. B* **1991**, *44*, 943. Liechtenstein, A. I.; Anisimov, A. I.; Zaanen, J. *Phys. Rev. B* **1995**, *52*, 5467.
(48) Leung, K.; Nielsen, I. M. B.; Kurtz, I. *J. Phys. Chem. B* **2007**, *111*, 4453.
(49) Cramer, C. J.; Truhlar, D. G. *Phys. Chem. Chem. Phys.* **2009**, *11*, 10757.

10184 *J. Phys. Chem. A, Vol. 114, No. 37, 2010*

Leung et al.

(50) Frisch, M. J. et al. *Gaussian 03, Revision E.01*, Gaussian, Inc.: Wallingford, CT, 2004.

(51) Kresse, G.; Furthmüller, J. *Phys. Rev. B* **1996**, *54*, 11169. Kresse, G.; Furthmüller, J. *Comput. Mater. Sci.* **1996**, *6*, 15.

(52) Kresse, G.; Joubert, D. *Phys. Rev. B* **1999**, *59*, 1758.

(53) Becke, A. D. *J. Chem. Phys.* **1993**, *98*, 5648.

(54) Lee, C. T.; Yang, W. T.; Parr, R G. *Phys. Rev. B* **1988**, *37*, 785.

(55) Perdew, J. P.; Burke, K.; Ernzerhof, M. *Phys. Rev. Lett.* **1996**, *77*, 3865.

(56) Schwegler, E.; Grossman, J. C.; Gygi, F.; Galli, G. *J. Chem. Phys.* **2004**, *121*, 5400. Sit, P.H.-L.; Marzari, N. *J. Chem. Phys.* **2005**, *122*, 204510. Rempe, S. B.; Mattsson, T. R.; Leung, K. *Phys. Chem. Chem. Phys.* **2008**, *10*, 4685.

(57) AIMD potential of mean force calculations have been shown to converge to within numerical noise for glycine tautomerization in water using a simulation cell smaller than the one used herein. See: Leung, K.; Rempe, S. B. *J. Chem. Phys.* **2005**, *122*, 184506.

(58) Reiher, M.; Salomon, O.; Hess, B. A. *Theor. Chem. Acc.* **2001**, *107*, 48.

(59) Ghosh, A.; Taylor, P. R. *J. Chem. Theory Comput.* **2005**, *1*, 597.

(60) Schultz, N. E.; Zhao, Y.; Truhlar, D. G. *J. Phys. Chem. A* **2005**, *109*, 4388.

(61) Rovira, C.; Kunc, K.; Hutter, J.; Parrinello, M. *Inorg. Chem.* **2001**, *40*, 11.

(62) Jaworska, M. *Chem. Phys.* **2007**, *332*, 203.

(63) Leung, K.; Rempe, S. B.; Schultz, P. A.; Sproviero, E. M.; Batista, V. S.; Chandross, M. E.; Medforth, C. J. *J. Am. Chem. Soc.* **2006**, *128*, 3659.

(64) Leung, K.; Medforth, C. J. *J. Chem. Phys.* **2007**, *126*, 024501.

(65) Kulik, H. J.; Cococcioni, M.; Scherlis, D. A.; Marzari, N. *Phys. Rev. Lett.* **2006**, *97*, 103001.

(66) Sit, P. H. L.; Cococcioni, M.; Marzari, N. *J. Electroanal. Chem.* **2007**, *607*, 107.

(67) Scherlis, D. A.; Cococcioni, M.; Sit, P. H. L.; Marzari, N. *J. Phys. Chem. B* **2007**, *111*, 7384.

(68) Referenes 65−67 apply the linear response DFT+U approach: Cococcioni, M.; de Gironcoli, S. *Phys. Rev. B* **2005**, *71*, 035105.

(69) Panchmatia, P. M.; Sanyal, B.; Oppeneer, P. M. *Chem. Phys.* **2008**, *343*, 47.

(70) Oppeneer, P. M.; Panchmatia, P. M.; Sanyal, B.; Eriksson, O.; Ali, M. E. *Prog. Surf. Sci.* **2009**, *84*, 18.

(71) As DFT+U calculations can be difficult to converge, we first use the robust Davison method in VASP ("IALG=38") to compute the Kohn−Sham wavefunctions of the first ionic step and then apply these as starting points to propagate subsequent molecular dynamics steps using the faster conjugate gradient ("IALG = 48") algorithm. Gas phase DFT+U calculations do not converge for some of the doubly negatively charged species.

(72) Sprik, M. *Chem. Phys.* **2000**, *258*, 139.

(73) Ivanov, I.; Chen, B.; Raugei, S.; Klein, M. L. *J. Phys. Chem. B* **2006**, *110*, 6365.

(74) Park, J. M.; Laio, A.; Iannuzzi, M.; Parrinello, M. *J. Am. Chem. Soc.* **2006**, *128*, 11318.

(75) Cheng, J.; Sulpizi, M.; Sprik, M. *J. Chem. Phys.* **2009**, *131*, 154504. Adruaabsem, C.; Sulpizi, M.; VondeVondele, J.; Sprik, M. *J. Am. Chem. Soc.* **2009**, *131*, 6046.

(76) Blumberger, J.; Klein, M. L. *Chem. Phys. Lett.* **2006**, *422*, 210.

(77) The same consideration should be used for the deprotonation $W(R)$. However, the reaction coordinate is more complex there, and R_{O-H} only varies by about 0.5 Å in that case; therefore the rotational prefactor $4\pi R_{O-H}^2$ varies less signficantly. We have not frozen any degrees of freedom in that calculation but have included a $4\pi R_{O-H}^2$ factor in the deprotonation free energy.

(78) See, e.g.: Chandler, D. *Introduction to Modern Statistical Mechanics*; Oxford University Press: New York, 1997; Chapter 6.

(79) Chandler, D. *J. Chem. Phys.* **1978**, *68*, 2959.

(80) Geissler, P. L.; Dellago, C.; Chandler, D.; Hutter, J.; Parrinello, M. *Science* **2001**, *291*, 2121.

(81) Laio, A.; Parrinello, M. *Proc. Natl. Acad. Sci. U.S.A.* **2002**, *99*, 12562.

(82) Iannuzzi, M.; Laio, A.; Parrinello, M. *Phys. Rev. Lett.* **2003**, *90*, 238302.

(83) Laio, A.; Gervasio, F. L. *Rep. Prog. Phys.* **2008**, *71*, 126601.

(84) Zhao, Y.; Truhlar, D. G. *J. Chem. Phys.* **2006**, *125*, 194101.

(85) Martin, M. G.; Thompson, A. P. *Fluid Phase Equilib.* **2004**, *217*, 105.

(86) Berendsen, H. J. C.; Grigera, J. R.; Straatsma, T. P. *J. Phys. Chem.* **1987**, *91*, 6269.

(87) Song, X.-Z.; Jaquinod, L.; Jentzen, W.; Nurco, D. J.; Jia, S.-L.; Khoury, R. G.; Ma, J. G.; Medforth, C. J.; Smith, K. M.; Shelnutt, J. A. *Inorg. Chem.* **1998**, *37*, 2009. Shelnutt, J. A.; Medforth, C. J.; Berber, M. D.; Barkigia, K. M.; Smith, K. M. *J. Am. Chem. Soc.* **1991**, *113*, 4077.

(88) Marzari, N.; Vanderbilt, D. *Phys. Rev. B* **1997**, *56*, 12847.

(89) Raebiger, H.; Lany, S.; Zunger, A. *Nature* **2008**, *453*, 763.

(90) Jaque, P.; Marenich, A. V.; Cramer, C. J.; Truhlar, D. G. *J. Phys. Chem. C* **2007**, *111*, 5783.

(91) Maximally localized Wannier functional analyses of CoP$^-$ and CoP^{2-} in water reveal that both species exhibit eight filled Co 3d spin-orbitals, consistent with a Co(I) charge state.

(92) Kumar, P. P.; Kalinichev, A. G.; Kirkpatrick, R. J. *J. Phys. Chem. B* **2009**, *113*, 794.

(93) Vchirawongkwin, V.; Pribil, A. B.; Rode, B. M. *J. Comput. Chem.* **2010**, *31*, 278.

(94) See, e.g.: Leung, K.; Rempe, S. B. *J. Am. Soc. Chem.* **2004**, *126*, 344.

(95) Daub, C. D.; Leung, K.; Luzar, A. *J. Phys. Chem. B* **2009**, *113*, 7687.

(96) Tossell, J. A. *Inorg. Chem.* **2009**, *48*, 7105, and references therein.

(97) The graphics package VESTA is used to generate Figure 3. See: Momma, K.; Izumi, F. *J. Appl. Crystallogr.* **2008**, *41*, 653.

(98) Peng, Z.; Merz, K. M., Jr. *J. Am. Chem. Soc.* **1992**, *114*, 2733. Peng, Z.; Merz, K. M., Jr. *J. Am. Chem. Soc.* **1993**, *115*, 9640.

(99) Asthagiri, D.; Pratt, L. R.; Kress, J. D.; Gomez, M. A. *Proc Natl. Acad. Sci. U.S.A.* **2004**, *101*, 7229. Tuckerman, M. E.; Marx, D.; Parrinello, M. *Nature* **2002**, *417*, 925. Tuckerman, M. E.; Chandra, A.; Marx, D. *Acc. Chem. Res.* **2006**, *39*, 151.

(100) Hammer, B.; Hansen, L. B.; Norskov, J. K. *Phys. Rev. B* **1999**, *59*, 7413.

(101) von Lilienfeld, O. A.; Tuckerman, M. E. *J. Chem. Theor. Comput.* **2007**, *3*, 1083.

(102) Campo, V. L.; Cococcioni, M. *J. Phys. Condens. Matter* **2010**, *22*, 055602.

(103) Wang, G.-T.; Dai, X.; Fang, Z. *Phys. Rev. Lett.* **2008**, *101*, 066403.

JP1012335